Optimization of GAMMASPHERE Data Following the Nuclear Reaction $^{36}\mathrm{Ar} + {}^{24}\mathrm{Mg} \longrightarrow {}^{60}\mathrm{Zn}^*$

Author
Paul Böhm

Supervisors
Dirk Rudolph
Yuliia Hrabar

A BACHELOR OF SCIENCE THESIS
FYSK03 WITH A DURATION OF 15HP
EXAMINED MAY 2023

LUND UNIVERSITY

DEPARTMENT OF PHYSICS
DIVISION OF PARTICLE AND NUCLEAR PHYSICS

Abstract

The experiment at Argonne National Laboratory aimed to study the fusion-evaporation reaction following the collision of a high-energy particle beam of ^{36}Ar with a stationary target of ^{24}Mg. This paper outlines the creation and implementation of an automated re-calibration procedure for the high-purity Germanium detectors comprising the GAMMASPHERE array used for γ-ray spectroscopy in this experiment. A Python script is used to compare the position of peaks in γ-ray spectra to known energy values, utilizing different methods of peak identification. Methods used in the procedure include the Gaussian fit, double Gaussian fit, and center of mass approach, and their accuracy in finding peak positions is compared. The procedure has shown an average decrease in detector array peak width of 6 % and immense time savings over manual re-calibration methods. Using data from the re-calibrated detectors, γ rays from the isomeric decay of ^{54}Fe are correlated and analyzed using γ-γ coincidence matrices in order to find possible γ rays stemming from yet unobserved transitions between excited states of ^{54}Fe. Further developments of the procedure include more in-depth considerations for the drift and non-linear behavior of some detectors, and how to rectify these phenomena.

Acknowledgements

I would like to thank my supervisor Dirk Rudolph for the guidance and support I was given during my thesis. It was Dirk who introduced me to the topic of nuclear physics, and his unmistakable passion for the field that led me to write my thesis with him. His quick and thorough feedback on my thesis drafts has been much appreciated and has helped me improve in many aspects.

To my co-supervisor Yuliia Hrabar, I extend my sincerest gratitude for all the explanations and countless hours of support with everything from technical problems to broader questions. All the help with the gits, ROOT files, and the GEBSort script is greatly appreciated, and I thank her for all of the help in analyzing the data together with Dirk.

Further, I wish to thank everyone from the Nuclear Structure Group for help in various matters and moral support. I must also extend my thanks to my dear friends, Jordis, Kim, Mel, Noah, and Sora, who wrote their theses alongside me and have supported me throughout my studies. I would not have made it this far without them. Lastly, I thank my family for their support and confidence in me during the course of my bachelor studies.

Contents

List of Acronyms

- **ANL** - Argonne National Laboratory
- **DAQ** - Data Acquisition System
- **DGS** - Digital Gammasphere
- **HPGe** - High-Purity Germanium
- **DSSD** - Double-Sided Silicon Strip Detector
- **FWHM** - Full-Width at Half-Maximum

1 Introduction

Since its discovery in 1911 by Ernest Rutherford, the atomic nucleus has been the central topic of study in the field of nuclear physics. It consists of so-called nucleons bound by the strong force, interacting very strongly over only a few femtometers. The nucleons present in the nucleus are divided into protons and neutrons, often occurring in approximately equal proportions or slightly neutron-rich. Protons have a positive electrical charge of $q = +1$, while neutrons are electrically neutral, leaving the overall nucleus with a positive charge equal to its number of protons. The number of protons and neutrons is used to differentiate and group different nuclei, giving rise to a proton number Z, neutron number N, and a total mass number $A = Z + N$.

When the proton number Z is plotted against the neutron number N, one obtains the nuclidic chart, as seen in fig. 1. This chart contains all known nuclei, most of which are unstable by nature. In order to minimize the energy inherent in the rest mass, the nucleus will decay towards the line of stability which is represented by the black squares in fig. 1 where different modes of decay are possible with certain probabilities. Though the line of stability follows $Z = N$ for light nuclei, it diverges toward a higher neutron number for heavy nuclei.

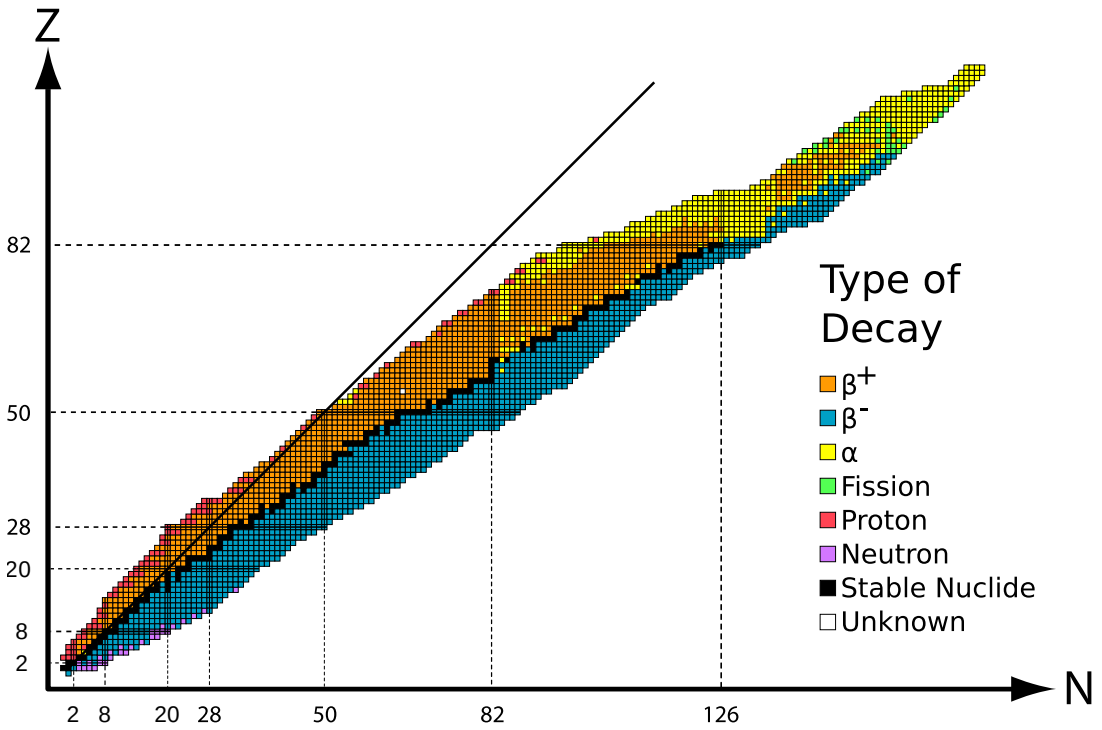

Figure 1: The nuclidic chart adapted from Wikimedia commons [1]. The proton number Z is plotted against the neutron number N, with the extra stable "magic numbers" labeled. The color represents the stability (black squares) or most probable mode of decay.

When diverging from the line of stability, one enters the neutron-deficient or neutron-rich domains where the most common decays are either β^+ or β^-. These decays are illustrated as orange and blue squares in fig. 1, respectively. Any decay will bring the nucleus closer to the line of stability, and will occur with a probability approximately proportional to

the distance from that line. Eventually, adding another neutron or proton to the nucleus will decrease the binding energy per nucleon, preventing the addition of this new nucleon. The lines on the nuclidic chart along which this occurs are aptly called the neutron or proton drip lines, effectively preventing the synthesis of nuclei beyond these lines.

To fill the nuclidic chart within these drip lines, and to characterize the decay of the associated nuclei, experimentalists aim to synthesize these neutron-deficient or neutron-rich nuclei. The nuclear reactions employed for this often involve the use of a particle accelerator, where excess energy is given to multiple nuclei upon collision, inducing nucleosynthesis. To detect the synthesis and subsequent possible decay of produced nuclei, detectors are placed around the collision site which record any resulting particles or radiation that is emitted. This thesis will treat the re-calibration and analysis of such a detector array, investigating mainly radiation stemming from a so-called fusion-evaporation reaction.

2 Theory

2.1 Fusion-Evaporation Reactions

A common nuclear reaction encountered in this thesis is the fusion-evaporation reaction. This is a phenomenon wherein the fusion of two atomic nuclei, usually as a result of collisions between accelerated nuclei, creates a short-lived compound nucleus. This nucleus will quickly decay through various means, as a result of the excess energy imparted to the nucleons and the resulting nuclear fragments such as α particles. The specific reaction channel will vary for a given individual compound nucleus, with a certain statistical probability for each possible decay. A pertinent example for this thesis is when ^{54}Fe is produced from an excited compound nucleus ^{60}Zn* as a result of the collision ^{36}Ar$+^{24}$Mg:

$$^{36}\mathrm{Ar} + {}^{24}\mathrm{Mg} \longrightarrow {}^{60}\mathrm{Zn}^* \longrightarrow {}^{54}\mathrm{Fe}^* + \alpha + 2p$$

Typically, the nucleus will first de-excite by means of particle evaporation, until a certain energy threshold has been reached. This entails the ejection of one or more nucleons, such as protons, neutrons, or even α particles. Next, the nucleus will decay by means of statistical γ rays until the yrast region is reached, which is its least excited state for a given angular momentum [2]. Lastly, discrete γ rays are released, stemming from the electromagnetic transitions between quantum states at low excitation energies of the residual nucleus. It is these γ rays that may be used to characterize the level scheme of the residual nucleus and assess its nuclear structure.

2.2 Excited States and Electromagnetic Transitions

One possible way to describe excited states in nuclei is to apply the nuclear shell model. It has proven particularly useful for nuclei with proton or neutron numbers close to the so-called "magic numbers" which mark large energy gaps between the shells of the shell model [3]. ^{54}Fe, the nucleus of interest here, has a proton number $Z = 26$ and a magic neutron number $N = 28$. When such a nucleus is excited, individual nucleons will become excited according to the nuclear shell model and move to a higher shell. These valence nucleons will determine the properties of the excited states of the nucleus, typically presented in terms of the inhabited shell and their parity.

When the nucleus undertakes a transition between an excited state and a lower-lying state, the resulting electromagnetic radiation, typically a γ ray, will have certain properties. These include the angular momentum L and an electromagnetic character σ to accommodate the quantum mechanical selection rules for nuclear spin and parity for a transition between initial state, $I_i^{\pi i}$, and final state, $I_f^{\pi f}$. The angular momenta and parities will determine the multipole characteristics of the emitted photon, with a given name of 2^L-pole. For instance, a γ ray representing an $E2$ transition would be characterized as quadrupole radiation caused by an oscillating electric field, which is known to conserve parity. The transition probability will vary significantly depending on the angular momentum, the energy of the γ ray, and the mass number A of the nucleus [4].

2.3 γ-γ Correlation Studies

When building decay schemes for nuclei a useful method is to use γ-γ correlations. This entails selecting γ rays of a certain energy and observing other possible γ rays that arrive at another detector coincidentally within an experimental time window of typically a few tens of nanoseconds. When the selected γ-ray energy is detected, the corresponding energy of accompanying γ rays are incremented in the column of the selected energy. This is consolidated into a so-called γ-γ matrix, where crossing rows and columns of γ-ray energies denote a correlation between the two γ rays. In this manner, γ-γ matrices allow one to isolate different branches of decay, and to build the decay scheme of nuclei.

2.4 Detection of γ Rays

The γ rays treated in this thesis are assumed to interact with matter in three main ways, as illustrated in fig. 2. In order to obtain an accurate γ-ray energy spectrum, it is vital to take each method of interaction into account such that all the energy in an event is accounted for. The cross-section of each interaction will vary with γ-ray energy. Roughly speaking, the low-energy regime is dominated by the photoelectric effect, the intermediate-energy regime is dominated by Compton scattering, and the high-energy regime is dominated by pair production [5].

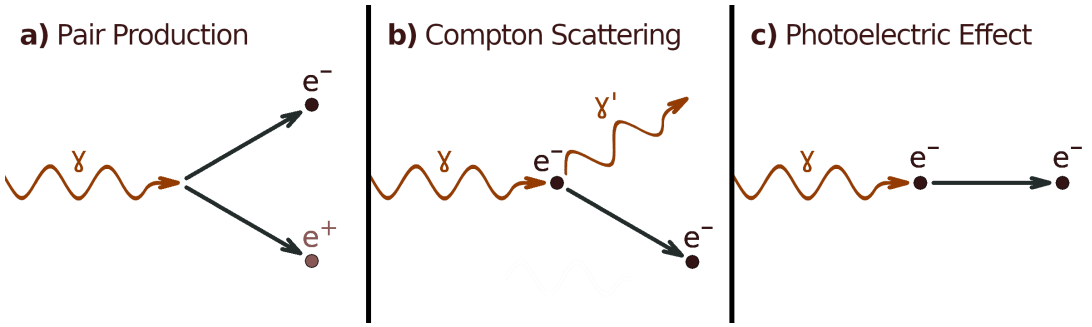

Figure 2: A schematic illustration of the three main ways in which γ rays may interact.

2.4.1 Pair Production

A γ ray of sufficient energy may generate an electron and its anti-matter equivalent, a positron. This requires the mass-equivalent energy of 511 keV for both the electron and positron, for a total of 1022 keV. The electron and positron travel inside the sensitive part

of the detectors, thereby releasing their kinetic energy. After depositing most of its kinetic energy, the interaction cross-section of the positron increases accordingly, typically resulting in annihilation with regular matter. This leads to the release of the mass equivalent energy of the annihilated electron and positron. When this process occurs in a detector, one or both 511 keV photons may escape, usually by two 511-keV photons emitted in opposite directions, causing a measured energy that is exactly 511 keV or 1022 keV less than expected. These are known as the single and double escape peaks.

2.4.2 Compton Scattering

When a γ ray of energy E_0 interacts with an electron in matter by giving the electron some energy and scattering off of it at an angle θ, it is known as Compton scattering. The new energy E of the γ ray is given by

$$E = \frac{E_0}{1 + \frac{E_0}{m_e c^2}(1 - \cos\theta)}$$

with an electron mass m_e and the speed of light c. This process is usually a source of background in spectra, as photons may deposit a continuous range of energies, depending on the scattering angle, or carry away energy when a γ ray scatters towards the outside of the detector before depositing all of its energy.

2.4.3 Photoelectric Effect

The photoelectric effect entails the complete absorption of a γ ray by the electron of an atom, given that the energy of the γ ray exceeds the ionization energy of the electron. When this occurs in a detector, the electron is ejected from an atom in the detector with a kinetic energy equal to the remaining energy after accounting for its binding energy. Usually, this kinetic energy is transferred to the detector material and measured.

2.5 High-Purity Germanium Detectors

High-Purity Germanium (HPGe) detectors are semiconductor detectors specialized for high-resolution γ-ray spectroscopy. They consist of one or more HPGe crystals. The semiconductor nature of Germanium stems from the fact that it has four valence electrons with a relatively low band gap of about 0.25 eV [6]. In the manufacture of semiconductor detectors, two types of regions are created, the n-type and the p-type regions. The n-type region is doped with atoms with an extra covalent bond available, such that electrons close to the conduction band will be filled into the doped state. The p-type region is instead doped with atoms with one less covalent bond, giving rise to another doped state close to the valence band of Germanium. This allows valence electrons in this region to be easily excited into the doped state, leaving behind holes with a positive charge. In the region connecting the doped materials, electrons introduced by doping the n-type region will migrate to the holes created in the p-type region, as seen in fig. 3. This is the depletion region of the semiconductor, where charges are stationary.

Photons which strike this region are detected as they dislodge electrons and holes, which are subsequently accelerated in the electric field applied across the depletion region. The amount of energy deposited in the semiconductor is proportional to the number of free electrons generated, which gives rise to a measurable pulse. Given the small band gap

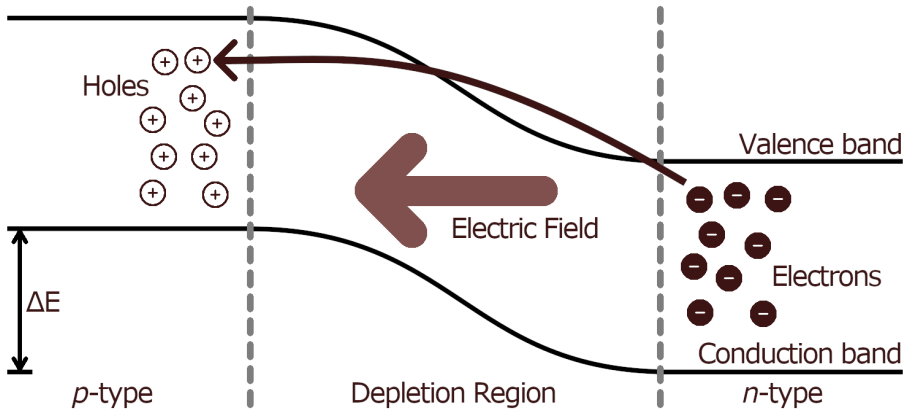

Figure 3: An image describing how the semiconductor is made. When the n-type and p-type regions are connected, the excess electrons of the n-type material migrate towards the excess holes of the p-type material, creating a depletion region. After the electron migration, an electric field is created pointing from the now electron-poor n-type material to the now electron-rich p-type material.

of semiconductor detectors, a lot of electron-hole pairs are generated for a given photon energy, giving rise to the high energy resolution semiconductors are known for. To improve the efficiency of the detector a larger depletion region is desirable, as only photons that hit this specific region will give rise to a pulse. This may be achieved by applying a reverse voltage to the semiconductor, expanding the electric field of the depletion region. Thermal excitations of electrons are a major source of noise, as small pulses may be created. To prevent this, the semiconductor crystals are often cooled well below room temperature using, for example, liquid nitrogen.

Next, the pulse generated by the detector is typically pre-amplified, amplified, and further processed, to finally give a voltage or current output which is readable by a computer. This output is proportional to the detected energy and discretized into bins for certain voltage or current ranges. For this thesis, the size of the bins treated is 1 keV in width. Next, the bins are calibrated to correspond to the correct energy, however, this calibration can drift over time, requiring re-calibration.

2.6 Energy Resolution and FWHM

When measuring a specific γ-ray energy, there typically is a spread in energies that is measured in the shape of a Gaussian curve. To determine the position and spread, one can fit a Gaussian curve on top of some background, utilizing the variables of the fit. The Gaussian distribution used in this thesis has the form,

$$f(x) = Ae^{-\frac{(x-\mu)^2}{2\sigma^2}} \tag{1}$$

where A is the magnitude, μ is the position, and σ is the standard deviation of the Gaussian. The variables of interest are the position μ and the standard deviation σ which is useful in determining the uncertainty of the measurement. A typical Gaussian least-squares fitted to some data is shown in fig. 4.

Relating to the standard deviation σ of the Gaussian, is the Full Width at Half Maximum (FWHM) of the Gaussian. This value is the full width of the Gaussian at $A/2$, and one

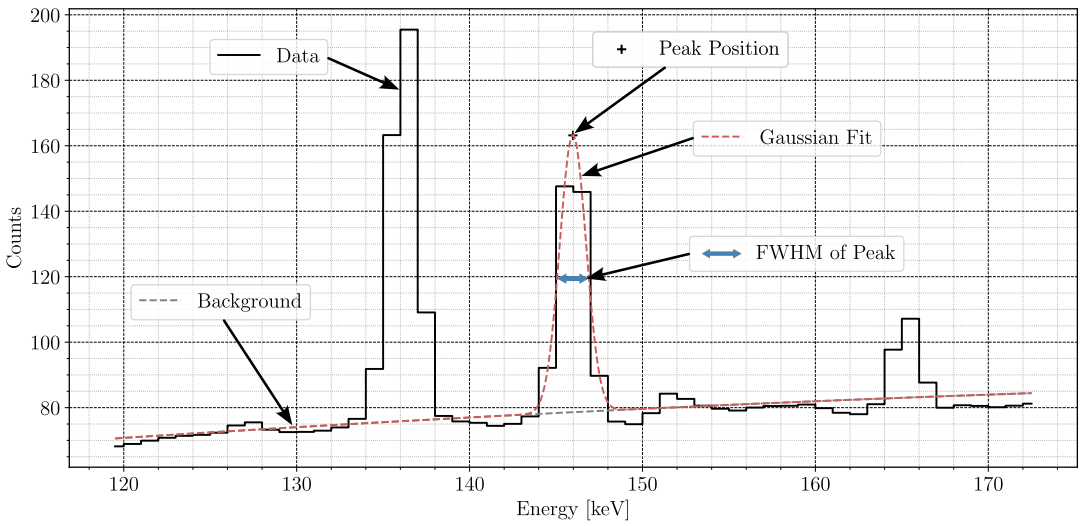

Figure 4: A typical γ-ray spectrum with an applied Gaussian fit on top of an arbitrary background. Relevant aspects of the plot are labeled and pointed out.

easily converts from standard deviation σ to FWHM by the following equation:

$$\text{FWHM} = 2\sqrt{2\ln(2)} \cdot \sigma \approx 2.355\sigma \tag{2}$$

The width of peaks will naturally increase at higher energies, which is accounted for in the resolution R of a detector. However, in this thesis, only the FWHM of the peaks is treated, along with the consideration at which energy the FWHM was achieved.

2.7 Calibration of Detectors

Calibration of detectors is used to correlate an output voltage or current reading, in the form of a bin number, with the correct energy. A good detector will have a linear relation between bin number and observed energy, which can be further refined by re-calibrations. A re-calibration is done by finding the position of certain peaks in the spectrum and adjusting the data such as to best match the observed peaks to their empirically known values. This is done through the use of a linear fit, where the best values for the linear coefficients k and m, as seen in the following equation, are found.

$$f(x) = kx + m \tag{3}$$

3 The Experiment

3.1 Experimental Setup

The experiment of interest for this thesis is an experiment conducted in 2020 at the Argonne National Laboratory (ANL), which entailed bombarding a thin foil of the isotope ^{24}Mg with a particle beam of ^{36}Ar accelerated to a kinetic energy of 88 MeV. The resulting compound nucleus was a highly excited form of ^{60}Zn* which rapidly decays using different means, as described in section 2.1. The setup is illustrated in fig. 5 and explained in more detail in the following section.

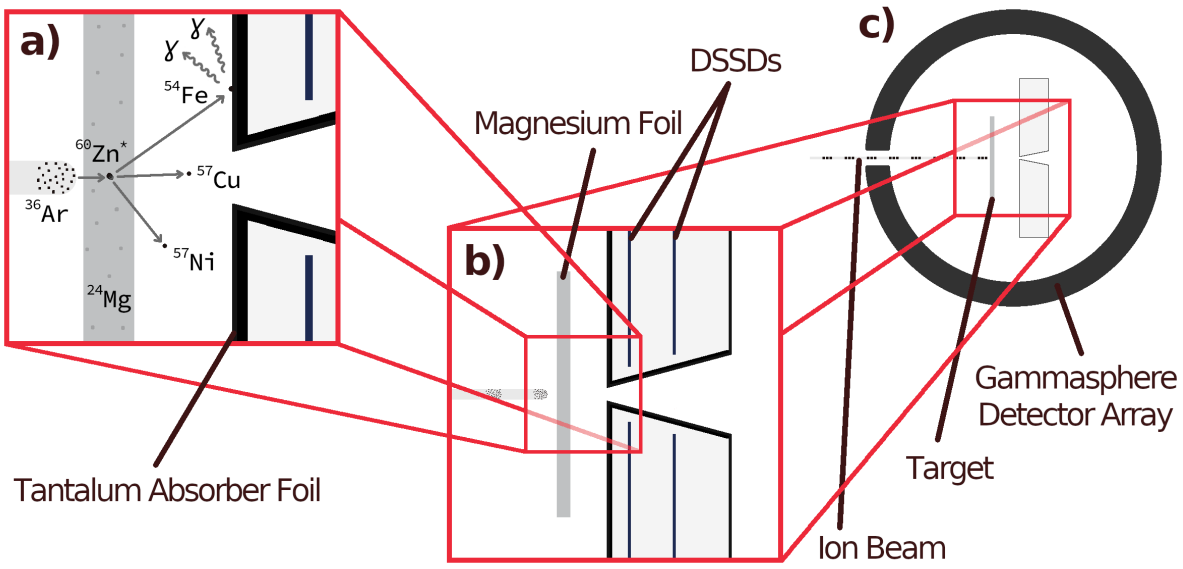

Figure 5: A schematic view of the Gammasphere target chamber and the components inside. The view is twice magnified in sections a), b), and c), where a) is the most magnified. A selection of possible nuclear reactions leading to observed γ rays is included.

Of particular use is the $1\alpha 2p$ reaction channel, which means that the initial highly excited nucleus of ^{60}Zn* emits one α particle and two protons. At relevant energies, this results in the creation of excited states in the nucleus ^{54}Fe. The energy relations of the preset $^{36}\mathrm{Ar} + {}^{24}\mathrm{Mg} \longrightarrow {}^{54}\mathrm{Fe} + \alpha + 2p$ reaction are such that the well-known 10^+ isomer in ^{54}Fe is reached, being a meta-stable state of the nucleus. This isomer decays with a half-life of $T_{1/2} = (364 \pm 7)$ ns by means of a sequence of usually five γ rays. This is documented in a proposed high-spin level scheme of ^{54}Fe [7], shown in fig. 6. In the process of de-excitation, the nucleus will emit a characteristic photon with an energy equal to the energy difference between the respective states. The emitted photons are subsequently detected by an HPGe detector array called the Gammasphere which surrounds the ^{24}Mg target. The set-up also comprises other detectors inside the target chamber, namely two double-sided silicon strip detectors (DSSD) and Microball CsI(Tl) scintillators for the detection of evaporated charged particles. The DSSD and CsI(Tl) detectors are protected with thin Ta foils against primary beam hits. Among other things, the function of these other detectors is to determine the reaction channel that was taken by the compound nucleus event by event.

Using the known energy of γ rays emitted from known reaction channels, such as the ^{54}Fe isomeric state, it is possible to re-calibrate the Gammasphere detectors as a function of time. Due to the extensive time period during which the detectors were utilized for the 2020 campaign, drift of the measured energy is inevitable in the detectors. The goal is to keep the energy peaks of the spectra aligned over time, through regular re-calibration.

3.2 The Gammasphere

The Gammasphere is an array of up to 110 high-purity Germanium detectors [8], which specialize in the detection of γ rays. To effectively identify the decay scheme of unstable nuclei the Germanium detectors have characteristically high energy resolution, meaning that they excel at differentiation of γ rays with different energies, as described in section

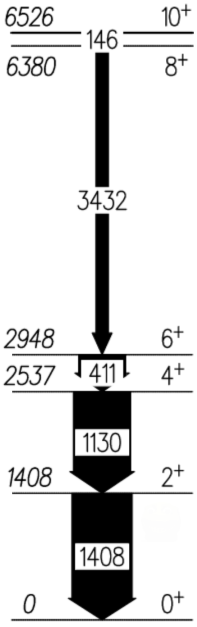

Figure 6: Part of the proposed high-spin level scheme of ^{54}Fe, adapted from [7]. Energies of the excited states and γ rays are in keV.

2.5. The detectors are placed around the experiment in a spherical configuration in order to detect as many γ rays as possible.

For the set-up used for the 2020 campaign, 32 germanium detectors were removed to make room for other detectors, such as a shell for neutron detection. Another component of the Gammasphere array detectors is the anti-Compton shielding. This shielding is useful in making sure that only γ rays that deposit all of their energy in the detector are considered. It works by omitting any measurements of when γ rays are detected outside of the Germanium detectors, as this indicates that they scattered out and left with some of their remaining energy.

3.3 Doppler-Shifted Lines

One notable property of the γ-ray spectra is certain lines that appear diagonally across multiple detectors over the spectrum. This relates to the fact that the residual nuclei such as ^{54}Fe, ^{57}Ni, or ^{57}Cu [see section a) of fig. 5] emit γ rays while they are moving at velocities of 3-4 % of the speed of light. Hence, a Doppler shift will occur to the emitted γ ray, causing a spread of energy depending on the angle θ between the path of the nucleus and the detector. To correct for this at velocities $v \ll c$, one can use the equation

$$E_\gamma = E_{\gamma 0}\left(1 + \frac{v}{c}\cos\theta\right)$$

which will adjust the detected energy for the Doppler shift. Here, E_γ is the actual energy, $E_{\gamma 0}$ is the energy at rest, and v is the speed of the nucleus.

4 Method

4.1 Data Acquisition System

In order to increase statistical significance several subsequent runs are selected and merged, making up a subset of data to be re-calibrated. On top of a base calibration, a re-calibration will be applied in *GEBSort* using a re-calibration file, which will be generated externally through the use of Python scripts. *GEBSort* is the main code handling the Digital Gammasphere (DGS) data, running in ROOT. The general idea of the re-calibration program is to automatically identify peaks of known energy in the spectrum of the Gammasphere detectors and compare their observed energy to the empirically known value (see fig. 6). A linear fit is used to correlate the known and observed energies, writing the parameters of the fit to a calibration file for each detector. The energy peaks used in the re-calibration are the following:

- **146 keV**: ^{54}Fe transition from the 10^+ isomeric state to the 8^+ state.
- **511 keV**: Signal from annihilation of positrons primarily from β^+ decay.
- **3432 keV**: ^{54}Fe transition from the 8^+ state to the 6^+ state, following the 146 keV transition mentioned above.

In this manner, the peaks for each detector are aligned to create a peak, that when summed over all roughly 70 active detectors, is as narrow as possible. An uncertainty of less than ± 0.1 keV for the given energy of the peaks is desired.

To achieve this, the goal is to develop a Python script that automatically fits Gaussians to the selected peaks in the energy spectra of the various detectors. Naturally, this script will not be viable in all situations, where some outliers may be treated manually if an automatic fit fails. Once the peak values are known, a linear fit can be made to correlate the detector bins to actual energy values. Thus, in order for a good final calibration to be obtained, the position of the peaks in the detector data need to be determined to a high level of accuracy, calling for reliable methods of peak identification.

4.2 Fitting Methods

To identify the positions of the peaks, three main methods are employed. These are the Gaussian fit, the double Gaussian fit, and the center of mass approach. Each method is suited to be able to best find the peak position given the shape of the peak and its surroundings.

4.2.1 Gaussian Fit

The most common type of peak identification is through the fitting of a Gaussian to certain parts of the data. As is seen in figs. 7 and 8, a small section of data around the suspected peak is evaluated, where the Gaussian is fitted along with a parabolically approximated background. In order to obtain accurate fits, the various parameters of the fit are automatically bounded. The fit is subsequently evaluated using the difference in height between the fitted peak and the data, and if results are below an adjustable

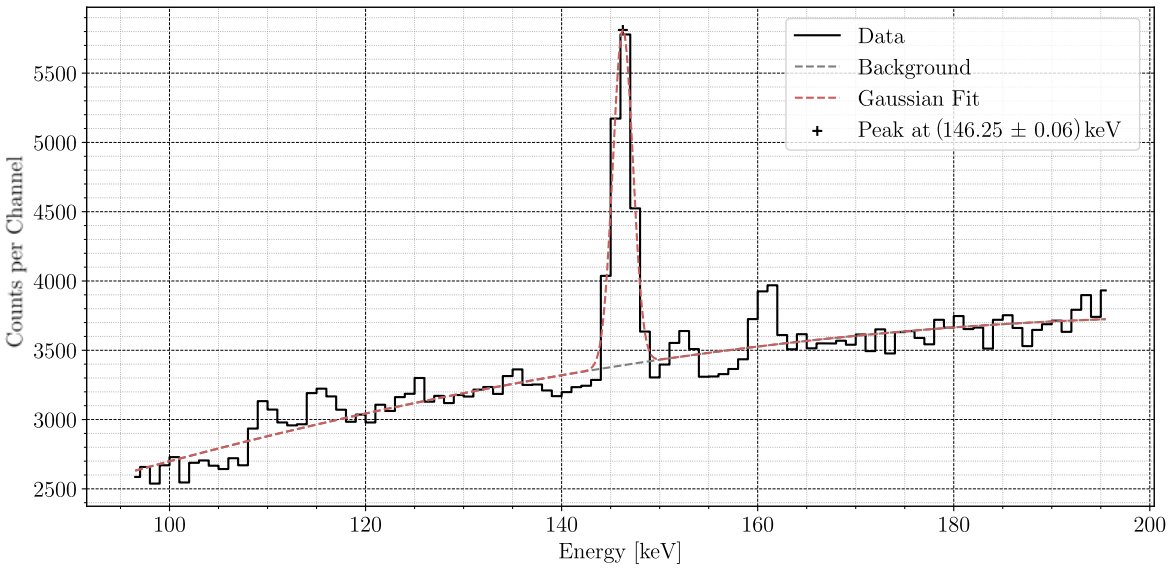

Figure 7: An example of a peak around 146 keV fitted as a Gaussian (red, dashed) on top of background (gray, dashed), which is here approximated to be of parabolic shape.

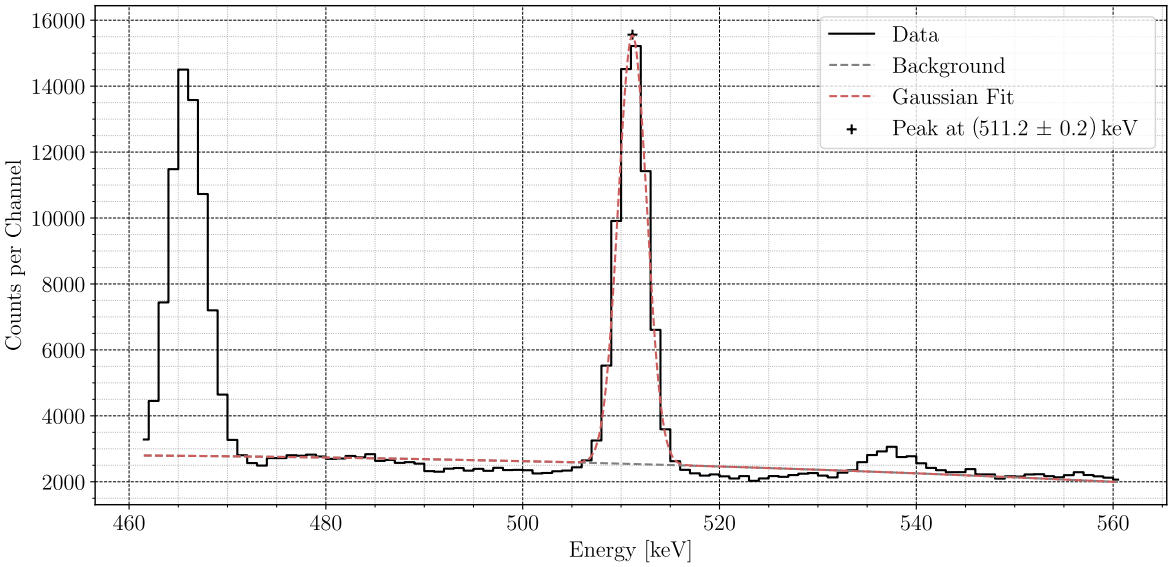

Figure 8: An example of a peak around 511 keV fitted as a Gaussian (red, dashed) on top of background (gray, dashed), which is here approximated to be of parabolic shape.

threshold the program will retry the fit with different parameters.

This method for peak identification is used for peaks that have the approximate shape of a Gaussian, such as the one seen in figs. 7 and 8, which are the peaks at 146 keV and 511 keV, respectively. These peaks typically have a large enough statistical weight to be modeled as Gaussians.

4.2.2 Double Gaussian Fit

When there is another significant peak in close proximity to the peak selected for fitting, it is useful to include the extraneous peak in the fit. This prevents the background fit from accounting for the peak and prevents the selected peak to be fitted to other extraneous peaks in the data. An example of this method being useful is shown in fig. 9, where the selected 146 keV peak is right next to the intense 136 keV peak emitted from excited states of Ta [see again fig. 5a)]. The usage of the double Gaussian fit in this scenario prevents a situation wherein the more intense 136 keV peak is mistaken for the 146 keV peak by the Python script.

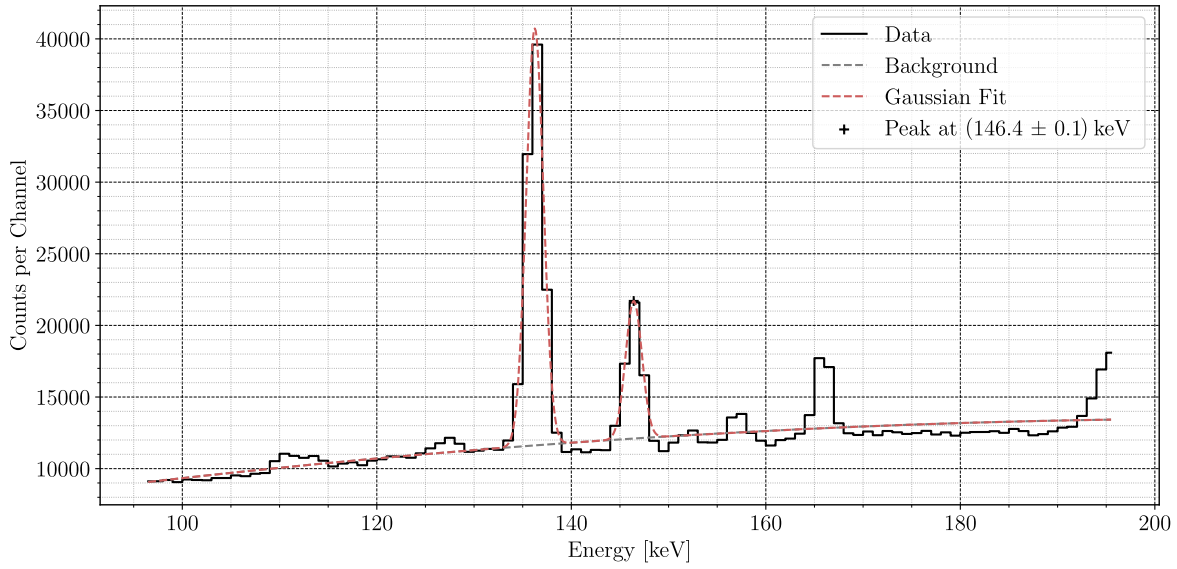

Figure 9: An example of a significant peak near the selected 146 keV peak to be fitted as a double Gaussian (red, dashed) on top of background (gray, dashed), which is here approximated to be of parabolic shape.

4.2.3 Center of Mass

For some peaks a Gaussian fit is not the most optimal choice. Peaks with low statistical weight, such as the peak seen in fig. 10, do not entirely match the shape of a Gaussian. These peaks come from detectors suffering neutron damage, a process where neutrons from the nuclear reaction get absorbed by the detectors and damage them. The small statistics gathered from these peaks compound the problem, ultimately leading to a smeared-out peak.

In cases like these, a center of mass approach will give a more appropriate estimation of the peak position, as a broader area around the peak is taken into account. This method will first find the background level, indicated in red in fig. 10, and then find a weighted average, shown in blue, from the background-subtracted peak shown in gray.

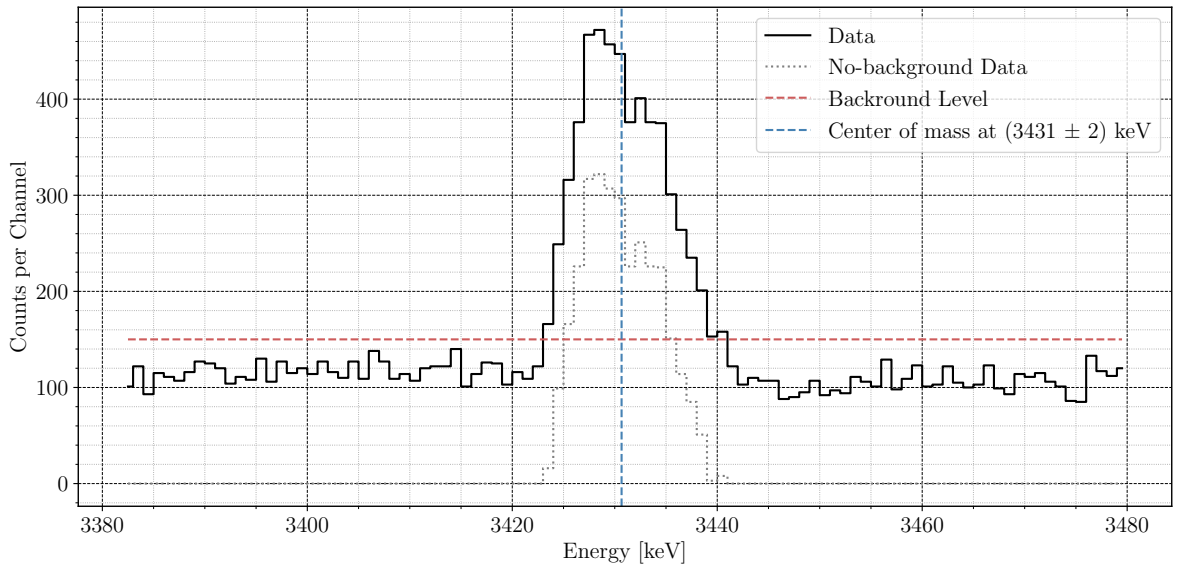

Figure 10: An example of a peak position (blue, dashed) found using the center-of-mass approach with a removed background level (red, dashed).

4.3 γ-γ Matrices and Spectra

In order to find γ rays in coincidence with the production of ^{54}Fe, a γ-γ matrix of the complete dataset is created, where all γ rays are plotted against each other as described in section 2.3. In this matrix, the lines intersecting the 146 keV line will stem from other γ rays that were detected coincidentally to the 146 keV γ ray. Next, the 146 keV γ ray is pre-selected, making another γ-γ matrix from the γ rays that arrived in the detector coincidentally, once a γ ray of energy 146 keV is detected. This matrix is only incremented when a γ ray multiplicity of three or more is achieved, requiring that one of the γ rays arriving at the detector falls in either the bin corresponding 145 keV or 146 keV. The total γ-γ matrix and the 146 keV pre-selected γ-γ matrix, also called the ^{54}Fe γ-γ matrix, are automatically generated by the *GEBSort* script. This is done in order to see previously unobserved γ rays following the decay of the isomeric state 10^+ to 8^+ of ^{54}Fe, such as $E4$ transitions from the 6^+ to 2^+ state or the 4^+ to 0^+ state. One may also observe a side branch from the 8^+ state of ^{54}Fe.

In order to get a clean 146 keV pre-selected γ-γ matrix, the background needs to be subtracted from this 146 keV matrix, generated from γ rays arriving at the detector in the bins corresponding to energies just below and above the peak energy. This should remove any γ rays that are not actually coincident with the isomeric decay of ^{54}Fe. In this ^{54}Fe γ-γ matrix, lines stemming from the decay of isomeric ^{54}Fe can further be projected to a 1D spectrum, showing γ rays coincident to the selected line. Again, one should perform a clean-up of the spectrum by removing the background. This spectrum around a certain line is similarly generated by selecting bins in the ^{54}Fe γ-γ matrix corresponding to the energy of the desired line, and subtracting from it the bins corresponding to the background energies just above and below the line. In addition to the γ-γ matrices, this will yield a spectrum of the total γ-ray coincidences with 146 keV γ rays, and a spectrum of the γ rays coincident with a peak from the isomeric decay of ^{54}Fe, here chosen to be the 1408 keV peak (see fig. 6).

5 Analysis and Results

Next, the results from the peak fitting and re-calibration are presented, along with an analysis and discussion thereof. Further, the spectra from the γ-γ correlation are shown and evaluated as to what they entail for the decay scheme of ^{54}Fe.

5.1 Peak Fitting

For the first subset, consisting of data from a total of eleven runs, the Gaussian method was used to automatically re-calibrate the energy spectra. The pre-calibrated spectra are seen to the left in fig. 11, and the subsequently re-calibrated spectra are seen to the right. With the combined statistical weight of eleven runs, the peaks at 146 keV and 511 keV were able to be fitted well using the Gaussian method, as is reflected in the well-aligned final spectra.

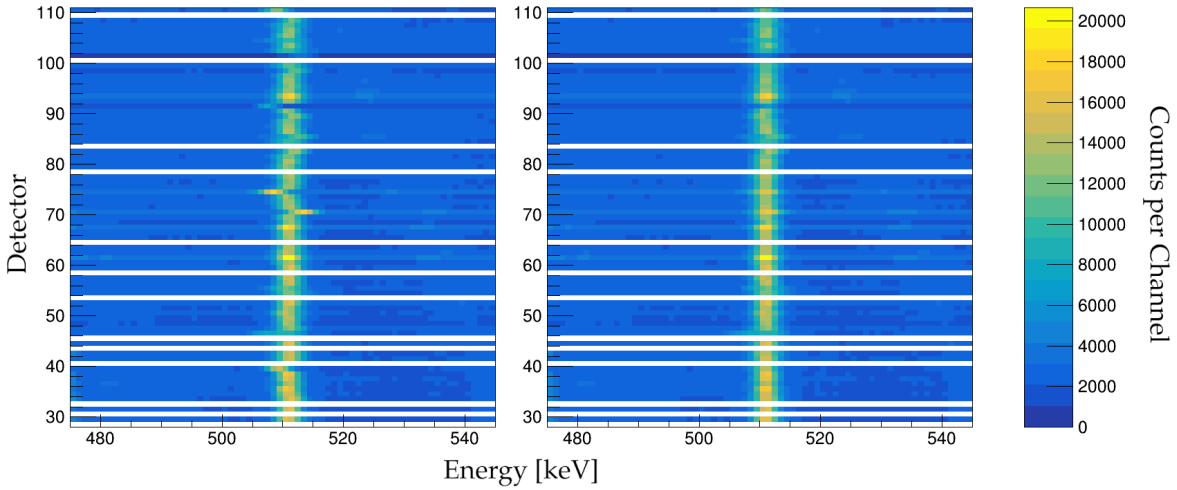

Figure 11: The pre-calibrated (left) and re-calibrated using a Gaussian fit (right) energy spectra around the 511 keV peak, for every active Gammasphere detector in the first subset of the data.

However, for the 3432 keV peak there was some degree of difficulty in fitting Gaussians to the peaks. This was due to the broad nature of the peaks, where using a Gaussian curve often results in a bad fit. Taking a closer look at the 3432 keV peak obtained for each detector using the Gaussian method on the left in fig. 12, it is evident that the peaks are often significantly smeared-out, compared to the peaks at 146 keV and 511 keV. A possible explanation for this is the relatively low intensity of the peak, with a maximum of about 600 counts, compared to typically 20000 counts in the 511 keV peaks. Another factor at play might be neutron damage to the Gammasphere detectors, building up over the lifespan of the detector. The result is somewhat misshaped peaks, which are hard to fit using the standard Gaussian method. This leads to uncertainty over the energy of the peak, consequently giving a worse re-calibration.

To somewhat remedy the smearing effect of higher energy peaks the automatic energy re-calibration was modified to allow for separate peak identification, in turn allowing the 3432 keV peak to be found using the center of mass approach. As can be seen on the

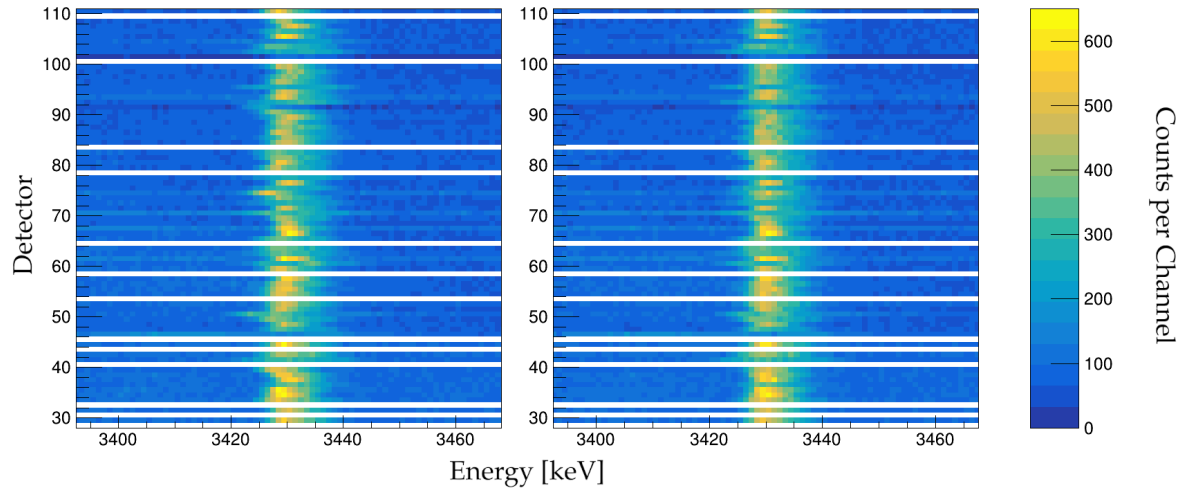

Figure 12: The re-calibrated energy spectra around the 3432 keV peak fitted using the Gaussian approach (left) and the center-of-mass approach (right), for every active Gammasphere detector in the first subset of the data.

right of fig. 12, this yielded somewhat better fits in the high-end of the spectrum, giving an overall better re-calibration.

Some detectors show a very broad peak at 3432 keV, such as the one seen in fig. 13, resulting in a worse estimate of the peak position. Such peaks are probably the result of a very badly neutron-damaged detector or a detector whose energy has drifted excessively over a short amount of time. The broad peak seen in fig. 13 seems to be composed of two distinct peaks, giving credence to the theory that this particular detector drifted excessively during the subset.

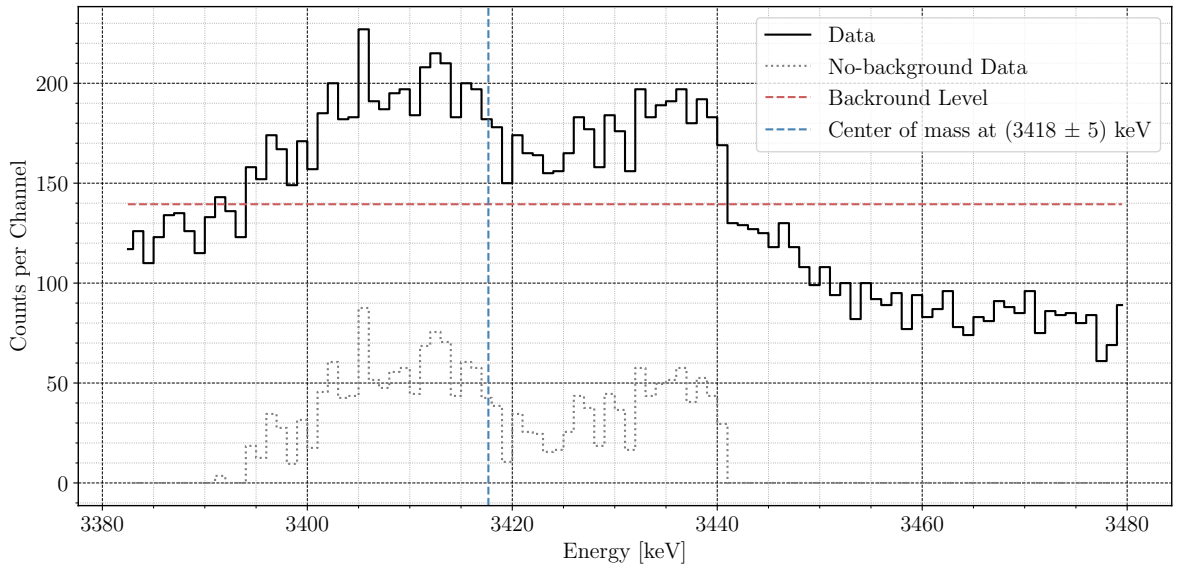

Figure 13: An example of a peak position (blue, dashed) found for detector 46 in the first subset using the center-of-mass approach on a very poor 3432 keV peak with a removed background level (red, dashed).

When detectors drift visibly, as seen in fig. 13, one can further divide the subsets and apply a separate re-calibration for each division. This was not done in this paper but would be an essential part of further data processing. During the re-calibration of the twelve subsets, significant drifting within subsets was noticed for detectors 46, 82, and 89. The drift observed for these detectors was as much as 20 keV in the first subset, and similar amounts for following subsets.

When excessive detector drift was observed, the accuracy of the peak fitting usually worsened. While the center of mass approach can deal with a slight drift, it is usually detrimental when coupled with the Gaussian method of fitting, due to the change in shape a peak undergoes when drifting within a subset. It should be noted that one should not include the affected detectors for matters of precision, as the peak drift will usually cause poor fitting and calibration. However, for applications where higher statistics are favored, one may opt to include the affected detectors with the limitation of drift in mind. This is especially pertinent for peaks at lower energies, as the magnitude of the drift seems to roughly scale with energy.

In later subsets, another peak started to grow significantly in magnitude at approximately 136 keV. This is clearly illustrated in fig. 7 where no significant peak is seen around 136 keV, when compared to fig. 9 where the 136 keV peak is almost twice as intense as the 146 keV peak. Due to the close proximity to the designated 146 keV peak, the 136 keV peak cannot be ignored, as the fitting script may mistake the peaks with each other. Additionally, the background may attempt to compensate for the extraneous peak, leading to a worse or wrongly placed background fitting.

For affected subsets, the double fitting method was employed with limited success. Without specified conditions on where the extra peak is located relative to the position of the wanted peak, either of the employed Gaussian fits could adhere to the wanted peak, or to irrelevant parts of the background. To remedy this, the condition that a second peak must be found around 10 keV below the wanted peak was added, resulting in a drastically increased rate of successful fitting.

One suggested improvement to the method could be to fit this 136 keV peak in addition to or instead of the 146 keV peak. However, this was eventually decided against, due to the sporadic nature of the peak, including its highly variable intensity. As mentioned in previous sections, this peak stems from an excited state of Ta, originating from the tantalum absorbers from the setup (see fig. 5). The intensity of this peak is mainly a function of beam focus, as the excited form of Ta is produced when charged particles from the ion beam miss the exit of the absorber structure and hit the Tantalum absorbers. This causes a Coulomb excitation of the ^{181}Ta nucleus, which ultimately de-excites releasing γ rays with an energy of 136 keV and 166 keV, or, in parallel, 301 keV.

5.2 Calibration and Uncertainties

Once the relevant peak positions have been collected through the process of fitting, they are plotted against the empirically known peak positions. This yields a scatterplot of data points to which a linear fit is applied (see black crosses and red dotted line in fig. 14) in order to extract the linear re-calibration coefficients k and m.

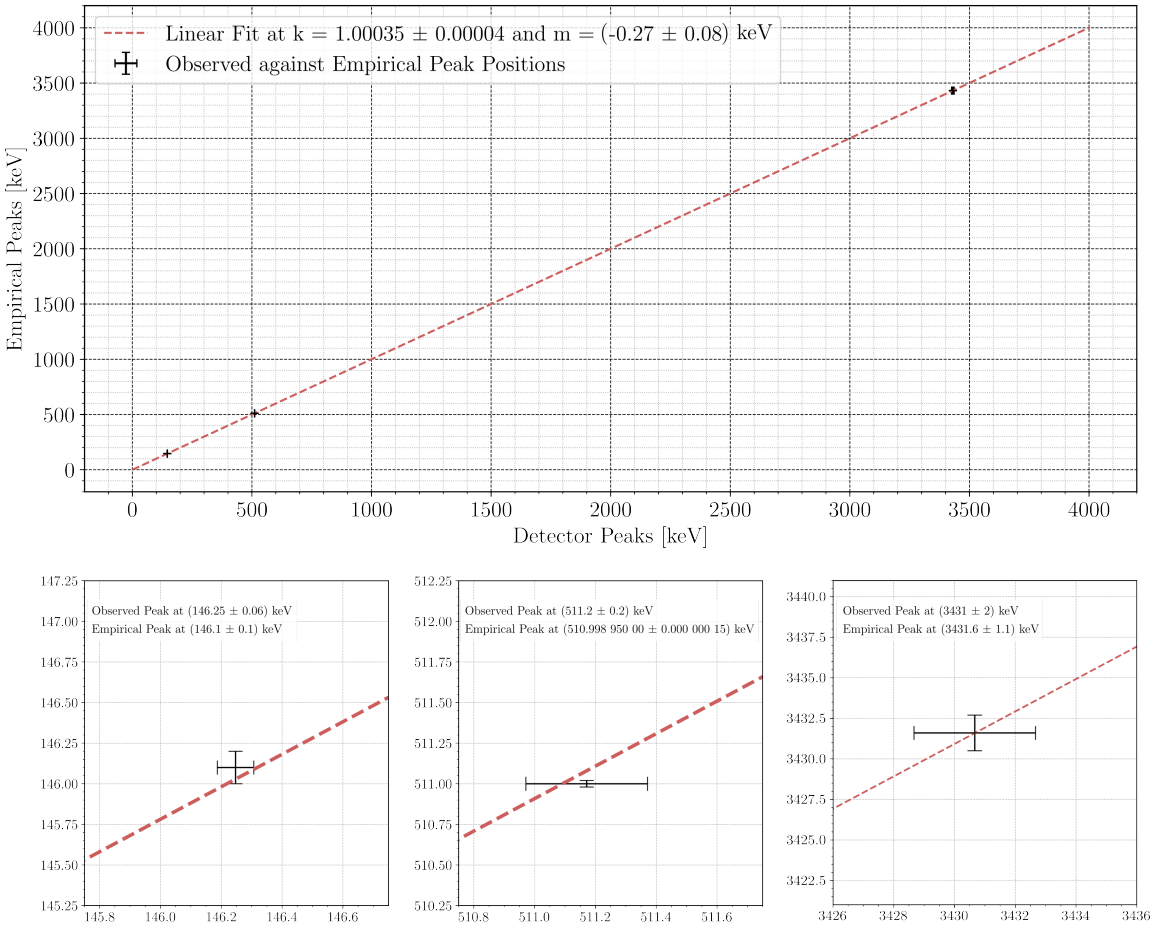

Figure 14: An example of the linear fit performed on the collected peak positions plotted against the empirically known peaks. Zoomed-in views around each data point are provided below, for a better view of the error bars. Linear fit and collected peak position uncertainties are obtained from the co-variance of the fit. The empirically known peak position uncertainties are taken from [7] and [9].

The uncertainties of the observed peaks are extracted from the co-variance matrix provided by the Python fitting package *SciPy* and are thus a function of how well the fit adhered to the data. The uncertainties of the empirical peaks come from literature, where the 146 keV and 3432 keV peak uncertainties come from [7], and the well-known 511 keV positron annihilation peak uncertainty can be found in [9]. For the linear fit, the re-calibration coefficient uncertainties are also derived from the co-variance of the fit, meaning it also indicates how well the fit adhered to the data.

To check the accuracy of the re-calibration, one can note how close the selected peaks are to their known energy values once the re-calibration is applied. This property mostly depends on how well the selected peaks are fitted and can be seen in fig. 15 by how close the overall merged peaks are from the known values before and after re-calibration. Here, one can observe that the accuracy is relatively good both before and after the re-calibration, with the exception of the 3432 keV peak. This is most likely due to the drift of certain

detectors, which is more prevalent at higher energies, as the uncertainty of a peak position should scale linearly with energy.

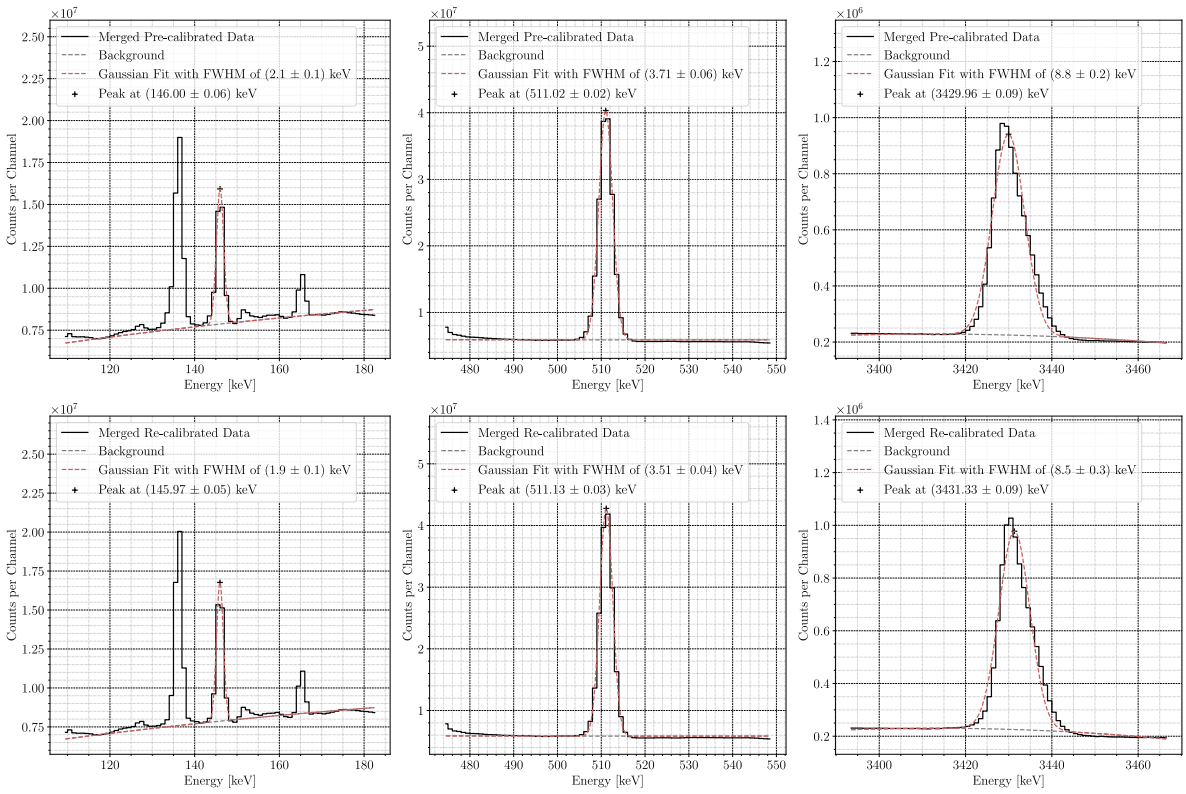

Figure 15: Data from all subsets, merged over all detectors to showcase detector alignment, around the 146 keV, 511 keV, and 3432 keV peaks. All peaks are fitted as a Gaussian (red, dashed) on top of a background of quadratic shape (gray), with their associated peak position and FWHM labeled. The data is shown before (top) and after (bottom) the re-calibration procedure.

The precision of the re-calibration, on the other hand, stems from the uncertainty of the linear fit coefficients, thus illustrating the confidence of the fit. Hence, this property will depend on how well the fit was performed, as explained above. However, it will also depend on the consistency and condition of the detector, as a linear fit is less likely to adhere well to data where a significant drift or damage is present. For most peaks, the precision will be dominated by the condition of the detector, since most peak positions can be fitted with a confidence on the order of $\pm$ 0.01 keV.

To ensure the absence of systematic errors, such as excessive drifting or damaged detectors, or faults in the re-calibration method itself, one can inspect the error bars of the peaks in relation to the linear fit. As seen in fig. 14, the linear fit performed on a typical detector will pass through the error bars of the various peaks. If the line would not pass through the error bars of all peaks, it would indicate that the data could not be fitted well, or that the uncertainties of the peak positions have been significantly underestimated. Most detectors passed this inspection, with the exception of when excessive drift was present, seen in detectors 46, 82, and 89 for instance, as described in previous sections.

The few detectors that did not pass the above-mentioned inspection seemed to not fit a linear calibration curve well, rather behaving in a non-linear manner. This problem typically manifested itself in that the detector alignment for all peaks was impossible using only a linear fit, especially at higher energies. Part of this behavior may be accounted for by the drifting peak positions and the accompanying drift in the linear calibration. However, the magnitude of the typically observed non-linearity far exceeds the magnitude of the drift, hinting at other factors involved. Most likely the non-linear behavior and the drifting are both symptoms of damage to the detector caused by the high-intensity radiation in its working environment. Another plausible explanation for the excessive drift may lie in changes in the experimental environment, as the electronics responsible for interpreting the signal may deviate in response to a change in temperature or placement, for instance. These changes might have been exacerbated due to the detector damage, causing an excessive drift.

The precision, and thus the degree to which random errors are minimized, of the re-calibration method can be translated into how well the detectors are aligned when viewed next to each other. This is depicted in figs. 11 and 12 from previous sections, where the precision of the Gaussian fitting method is demonstrated for the 511 keV and 3432 keV peaks, respectively. In summation, the accuracy and precision of the re-calibration method itself can be diagnosed, respectively, by seeing how close the re-calibrated peaks are to their known energies, and how well the peaks align over the different detectors.

5.3 General Observations

When the same peaks on all detectors line up well across all subsets, it will contribute to a sharper peak when the data is merged. This will increase the precision with which one can locate a peak and, in turn, increase the observed resolution of the detector. This is observed after the re-calibration in fig. 15, where the signal width, represented by the FWHM, has decreased for each peak. Comparing the FWHM before and after the re-calibration, one observes an average decrease of $(5.3 \pm 3.5)\%$ over the complete merged dataset. Though the peak width scales naturally with energy, one can still compare the fractional decrease in FWHM, as the energy dependency will cancel out.

The large error on this measurement stems from the way percentage change is calculated and the relatively small reduction in FWHM as a result of re-calibration. Consider the peak at 146 keV before and after re-calibration, where the FWHM changes from (2.1 ± 0.1) keV to (1.9 ± 0.1) keV (see the leftmost graph of fig. 15). The difference in FWHM would become (0.20 ± 0.14) keV, as the uncertainties are added under the square. When this difference is compared to the original FWHM to obtain a percentage change, the uncertainty will naturally be large. As explained in the previous section, the precision here is more of an indication of how well the Gaussian fit can adhere to the data. An uncertainty of ± 0.1 keV is reasonable in this case considering the energy resolution of 1 keV from the binning of the data.

To gauge how well the method aligned the detectors across the subsets, one can observe the FWHM of the peaks produced, as seen in fig. 16. The FWHM of each individual detector is plotted against the detector number for each peak, displaying several trends. Firstly, one can note that the FWHM clearly scales with energy, as the peak width strictly

increases at larger energies. This is due to the naturally decreased precision at higher energies, as described in previous sections.

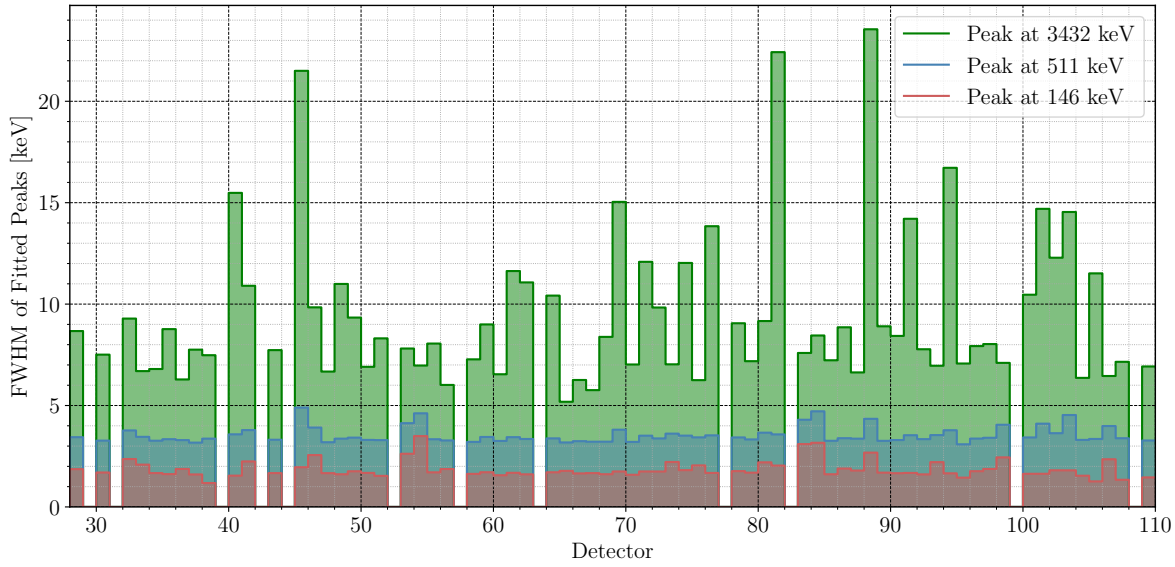

Figure 16: The FWHM of the 146 keV (red), 511 keV (blue), and 3432 keV (green) peaks fitted using re-calibrated data from all subsets, for each detector. The FWHM of each peak is shown in the same plot, and filled in for visibility. The inactive detectors 0-28 have been omitted, and further inactive detectors have been left blank.

Secondly, one can note that the FWHM for a given peak remains relatively constant around an average value, with the exception of the 3432 keV peak. This signifies a low spread in values and thus a good fitting precision. This behavior is further demonstrated in the average value of the FWHM for the peaks merged across all detectors and subsets in fig. 15, where the uncertainty of the FWHM is relatively low for peaks at 146 keV and 511 keV. Accordingly, the 3432 keV peak FWHM shows a higher uncertainty. This trend is seen because data merged from peaks fluctuating relatively little will yield a sharper, and better-shaped Gaussian, while data merged from a highly fluctuating peak is not only wider, but also more prone to a worse fit due to subsequent deformed Gaussian.

Lastly, given the fluctuating width of the 3432 keV peak, there are several detectors one could classify as outliers based on their especially large peak width. When selecting a cut-off point at FWMH = 20 keV, three detectors are noted. Unsurprisingly, they are detectors 46, 82, and 89, the same detectors that displayed excessive drift and borderline non-linear behavior at higher energies, discussed in the previous section. Given the unusually high peak FWHM for these detectors, it is prudent to remove them from the dataset for high-precision applications, to improve the final merged data. This is done in fig. 17, where the merged peaks are again fitted for the re-calibrated data.

As can be seen from this figure, the FWHM for the 3432 keV peak in particular has decreased somewhat from FWHM = (8.5 ± 0.3) keV to FWHM = (8.4 ± 0.2) keV, a decrease of about 0.1 keV. For the peak at 146 keV a similar decrease in overall peak FWHM is observed, but for the peak at 511 keV a slight increase is noted. While the overall FWHM

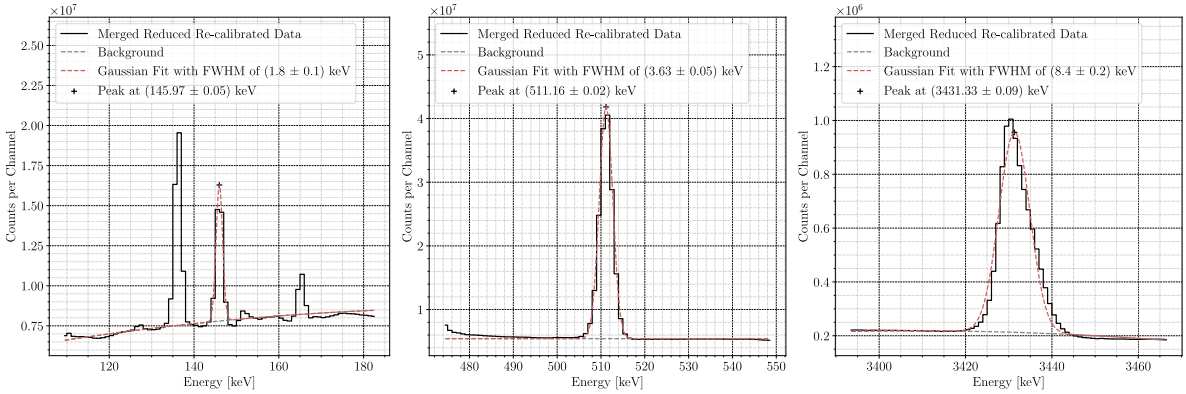

Figure 17: Data from all subsets, merged over all detectors around the 146 keV, 511 keV, and 3432 keV peaks. All peaks are fitted as a Gaussian (red, dashed) on top of a background of quadratic shape (gray, dashed), with their associated peak position and FWHM labeled. The data is shown after the re-calibration procedure and the removal of detectors 46, 82, and 89 from the dataset.

for the peaks decrease slightly when removing the worst detectors, it is barely significant enough to observe. This indicates that the faulty detectors do not contribute too much to the increase of the FWHM and that the driving factor for the FWHM rather lies with the composite of all detectors. Nevertheless, one observes an average decrease of $(6.1 \pm 3.3)\%$ over the pre-calibrated merged dataset, an improvement of about one percentage point.

When selecting peaks to locate for the re-calibration, a strong peak that has no overlapping peaks or significant noise is desirable. Due to the fact that some dislodged nuclei in the experimental setup are moving at high velocities (see fig. 5), some emission lines will be Doppler-shifted, depending on the angle at which the detector receives the γ ray. This leaves broad streaks over the spectrum across several detectors, preventing a good fit of affected peaks. This effectively reduces the number of peaks available for the re-calibration. An example of the skewed Doppler lines is seen in fig. 18, where all visible lines, except the 411 keV and 511 keV lines, are skewed.

5.4 γ-γ Correlation Results

When merging the complete data from the experiment, the resulting ^{54}Fe γ-γ matrix created by pre-selecting the 146 keV peak can be seen in fig. 19. When selecting a vertical or horizontal line, it does not matter which as the plot is mirrored, one can see which γ rays are detected coincidentally to it by the intersecting lines. For instance, one can see that the line at 3432 keV intersects with lines at 411 keV, 1130 keV, and 1408 keV, which is expected, as all these γ rays usually follow after the isomeric decay of ^{54}Fe.

The weak diagonal lines that can be observed in fig. 19 result from Compton scattering of γ rays within the detectors, which have evaded the anti-Compton shield by scattering at very high angles. The original energy from which the diagonal line stems is obtained by adding the energy on either axis at any point along the diagonal. This line fades out at low and intermediate energies on each axis, due to the nature of Compton scattering. At low energies, the cross-section of Compton scattering occurring is not significant compared to the photoelectric effect, as the γ ray is more likely to be completely absorbed.

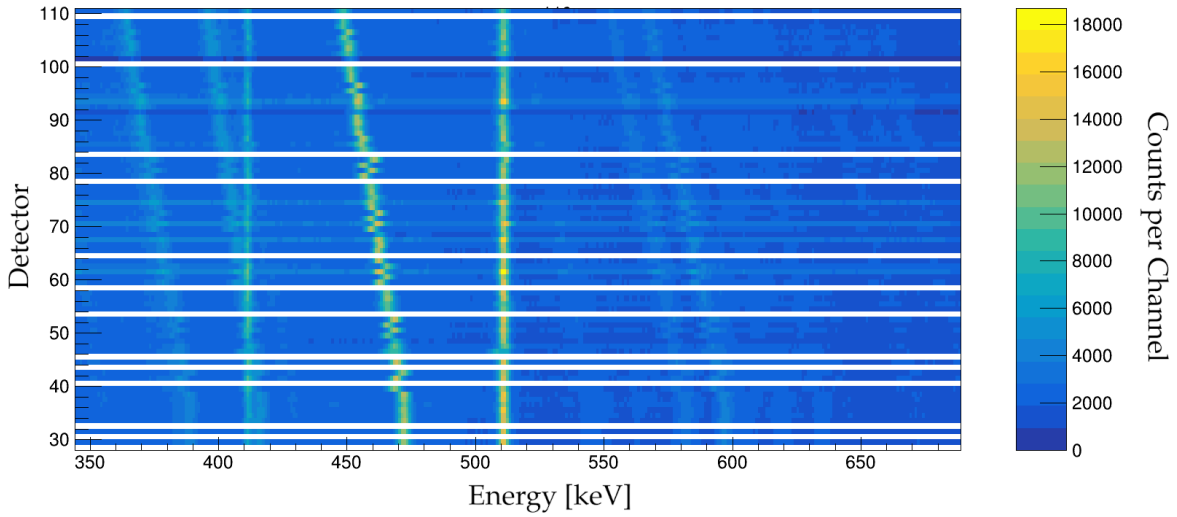

Figure 18: An example of the Doppler-shifted lines in the re-calibrated energy spectra around the 511 keV peak, for every active Gammasphere detector in the first subset of the data.

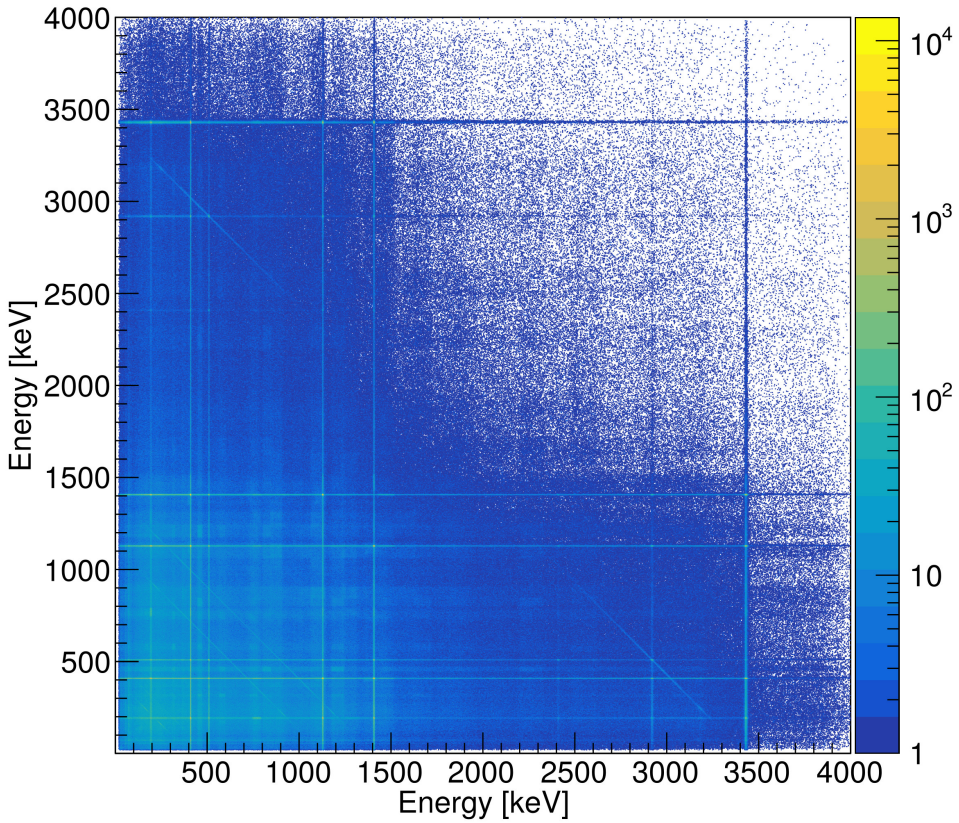

Figure 19: The ^{54}Fe γ-γ matrix produced through pre-selection of the 146 keV peak. The z-axis is in a log scale in order to better distinguish the lines. The figure was produced with help from Yuliia Hrabar.

At intermediate energies, there is too much energy in the γ ray to scatter with an angle close to 180°, allowing the anti-Compton shield to veto the event. This highlights a physical limitation in the anti-Compton shielding of the Gammasphere, in that the shielding cannot cover all angles of scattering and still allow entry of the γ rays.

When projecting the ^{54}Fe γ-γ matrix and its corresponding background matrix to 1D spectra one can see any γ rays coincident with the 146 keV γ ray. Subtracting the two from each other yields a cleaner spectrum where extraneous peaks are, in theory, removed. An example of this is seen in fig. 20 (left), where the small bump at around 460 keV is removed after the background subtraction. However, while the 511 keV peak is reduced in magnitude, it nonetheless remains despite not strictly being correlated with the 146 keV γ ray if solely originating from β^+ decay. This shows that the background selection may not be perfect with regard to the 146 keV peak, that the chosen coincidence time window is too large, or that the remaining yield at 511 keV stems from pair production interaction.

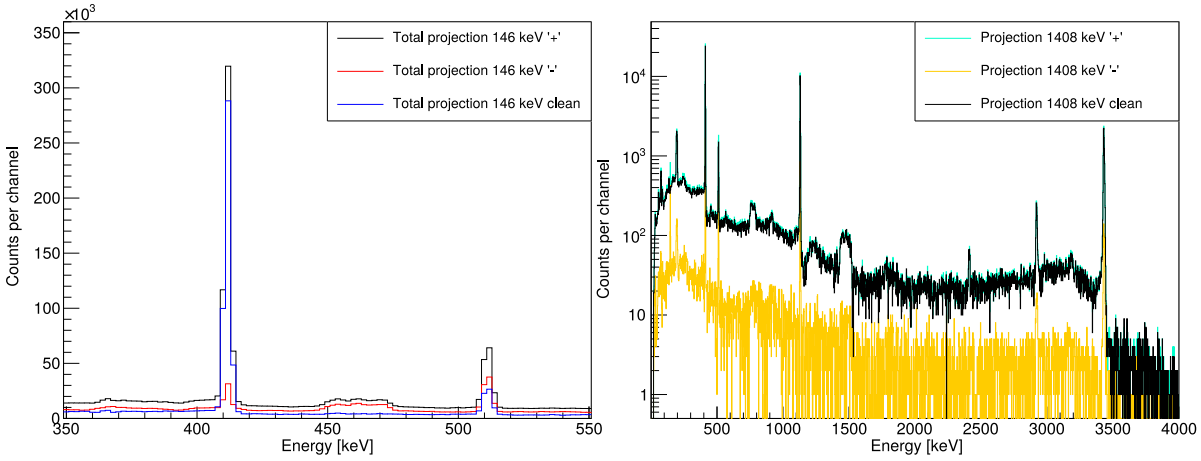

Figure 20: Part of the coincidence spectrum of all γ rays being detected together with a 146 keV γ ray (left), and the spectrum of the γ rays coincident with the 1408 keV peak from the isomeric decay of ^{54}Fe on a log scale (right). The spectra corresponding to the peak and background are marked with '+' and '-', respectively, resulting in a clean spectrum once subtracted from each other. The figures were produced with help from Yuliia Hrabar.

The spectrum obtained when selecting another γ ray in coincidence with the 146 keV peak can be seen in fig. 20 (right). The selected peak is the 1408 keV peak, which stems from the last decay in the isomeric decay sequence of ^{54}Fe. This spectrum will only show the γ rays which come in coincidence with the γ rays of energy 146 keV and 1408 keV. Due to the large range in counts among the peaks, a log scale has been selected for this figure, which allows for the identification of peaks with low and high statistical significance. As expected, one can see other peaks from the ^{54}Fe decay chain, such as the 3432 keV peak and its single and double escape peaks. Again, the 511 keV positron annihilation peak is visible due to the limitations of the coincidence matrix.

Yet unobserved transitions subsequent to the production of the 10^+ isomer of ^{54}Fe may include an $E4$ transition between the 6^+ to 2^+ states or the 4^+ to 0^+ states. These transitions would have the energies of $E = 411$ keV $+ 1130$ keV $= 1541$ keV and $E = 1130$ keV $+ 1408$ keV $= 2538$ keV, respectively. In fig. 20 (right), one should be able to see the E4 transition from the state 6^+ to 2^+ of energy 1541 keV, as it shows the γ rays coincident with the 1408 keV peak. Other possible undiscovered transitions stem from a side branch from the 8^+ state of ^{54}Fe that may occur with a very low probability. This branch may be seen in the coincidence matrix of 146 keV.

As it stands, these transitions have not been spotted with enough statistical significance in either plots in fig. 20. To possibly uncover these transitions the selection for the γ-γ matrix will have to be refined and experiments with more statistics may be run.

6 Outlook and Conclusion

In summary, data from an ANL experiment has been analyzed to generate re-calibration coefficients for the Gammasphere germanium detector array. This script used different methods of locating peaks in the Gammasphere spectra including the Gaussian fit, double Gaussian fit, and the center of mass method. The effectiveness of each method has been qualitatively described and quantitatively measured in terms of reduction in the FWHM of the peaks. Further, the detectors which were working sub-optimally were identified and removed from the dataset for better peak sharpness. Overall, an average reduction in peak FWHM of $(6.1 \pm 3.3)\%$ has been achieved. After the data re-calibration, several γ-γ matrices were made in order to study the decay chain of isomeric ^{54}Fe and possibly find hitherto unobserved transitions and branches of decay. Unfortunately, no such transitions have been found as of yet, but work on this is ongoing. To improve the re-calibration method and increase the precision and accuracy of the results there are several suggestions for future studies.

One improvement would be to remove the Doppler-shifted lines. To get rid of these lines, which may skew the fit of the energy peaks used for re-calibration, one may attempt to use off-prompt timing for future studies. Since the particle beam is incident on the target in pulses a few ns wide, arriving approximately every 80 ns, one may limit the detector statistics such that in-flight nuclei do not contribute to the γ-ray spectra. Further, one might cut off the earliest part of the data such that only γ rays from the stationary nuclei caught in the tantalum foils contribute to the spectra under investigation.

The removal of the Doppler lines would allow for the usage of more intense peaks in the re-calibration of the detectors, increasing accuracy and precision accordingly. The importance of finding the peak position of an individual peak would decrease when more peaks are available for fitting, making it such that a single badly fitted peak would have a limited effect on the overall re-calibration. With multiple peaks at hand, one could further choose to omit certain peaks when they are deformed due to, for instance, excessive drift. In this thesis, this would have allowed for the de-selection of the 3432 keV in the detectors where excessive drift was found, allowing for a better re-calibration.

One would also stand to improve the re-calibration by including more peaks in general, not just very intense peaks. While the peak position is found more easily in these peaks, utilizing a multitude of smaller peaks yields different advantages. For instance, having many smaller peaks would allow one to have a greater distribution of data points, allowing for more points of calibration throughout the spectrum. Ideally, one could combine the few intense peaks with a multitude of smaller ones, perhaps weighing the contribution to the calibration of each peak according to the confidence of the fit and the precision of the position. A weighted fit across each peak position according to its precision would further help in limiting the impact of drifting peaks and detectors.

Another possible improvement to the method would be to run the re-calibration on every single run individually, effectively eliminating, or at least further minimizing, the phenomenon of detector drift. Though the process of re-calibrating every run would be more time intensive, it is likely to yield more accurate re-calibrations.

Lastly, a future improvement to the method is to consider different equations for the re-calibration. In order to fix the non-linear behavior of some detectors, it might help to use a non-linear equation, such as a polynomial or exponential. One could also re-calibrate the affected detectors using a linear equation with incorporated departure coefficients in order to quantize how significant the non-linear behavior is and rectify it.

7 References

[1] Napy1kenobi. *Table isotopes.svg - Wikimedia Commons*. [Online; accessed 11. Apr. 2023]. May 2008. URL: https://commons.wikimedia.org/wiki/File:Table_isotopes.svg.

[2] J. Robb Grover. "Shell-Model Calculations of the Lowest-Energy Nuclear Excited States of Very High Angular Momentum". In: *Phys. Rev.* 157 (4 May 1967), pp. 832–847. DOI: 10.1103/PhysRev.157.832.

[3] Kenneth S. Krane. "Gamma Decay". In: *Introductory Nuclear Physics*. John Wiley & Sons Inc, New York, 1988.

[4] D. Rudolph. *HandOuts-part2.pdf: FYSC22 - Physics: Nuclear Physics*. [Online; accessed 8. May 2023]. May 2022. URL: https://canvas.education.lu.se/courses/16548/files/2468596.

[5] J. S. Lilley. *Interaction of radiation with matter: Gamma rays*. John Wiley & Sons Ltd, Chichester, 2001.

[6] Kenneth S. Krane. "Detecting nuclear radiations". In: *Introductory Nuclear Physics*. John Wiley & Sons Inc, New York, 1988.

[7] D. Rudolph et al. "Single-particle and collective excitations in the $N = 28$ isotones ^{54}Fe and ^{53}Mn". In: *Phys. Rev. C* 102 (1 July 2020), p. 014316. DOI: 10.1103/PhysRevC.102.014316.

[8] *Gammasphere | Argonne National Laboratory*. [Online; accessed 8. Feb. 2023]. Feb. 2023. URL: https://www.anl.gov/phy/gammasphere.

[9] *NIST CODATA Value: electron mass energy equivalent in MeV*. [Online; accessed 14. Apr. 2023]. May 2019. URL: https://physics.nist.gov/cgi-bin/cuu/Value?mec2mev.